Received 8 June 2023; revised 2 July 2023; accepted 12 July 2023. Date of publication 18 July 2023; date of current version 8 August 2023.

Digital Object Identifier 10.1109/OJAP.2023.3296623

Compact U6G Massive MIMO Antenna Arrays With Double-Layer Partial Reflective Decoupling Layers for Mutual Coupling Suppression

TING LIU[1], JIAYUE JIANG[1], LUYU ZHAO[1] (Senior Member, IEEE), GE ZHAO[1] (Graduate Student Member, IEEE), HUIQING ZHAI[1] (Member, IEEE), YUAN-MING CAI[1] (Member, IEEE), TEYAN CHEN[2], AND WENWEI XU[2] (Senior Member, IEEE)

[1]National Key Laboratory of Antennas and Microwave Technology, Xidian University, Xi'an 710071, Shaanxi, China

[2]Institute of Strategic Research, Huawei Technologies Company Ltd., Shenzhen 518129, China

CORRESPONDING AUTHOR: L. ZHAO (e-mail: lyzhao@xidian.edu.cn)

This work was supported by Huawei Technologies Company Ltd.

ABSTRACT In this paper, a systematic decoupling strategy of two partial reflective decoupling layers (PRDLs) and dummy decoupling probes (DDPs) is utilized to suppress the complicated couplings in a ±45° dual-polarized, compact antenna array operating at Upper 6 GHz (U6G, 6425–7125 MHz) bands. Finely engineered neutralization electromagnetic waves are introduced by two PRDLs to counteract the original couplings. Two layers of PRDLs are placed above the antenna array in a step-by-step manner to gradually cancel out several major couplings while DDPs are placed around the antenna elements to reduce the remaining couplings. The measurement results of the 6 × 4 staggered quadruple folded dipole (QFD) array prototype with power combiners show that within the U6G band, the isolations between all ports are improved to more than 21 dB with good port matching performance, while the radiation pattern and envelope correlation coefficient are also in good condition, which verifies the correctness and effectiveness of the proposed decoupling method, especially in very compact U6G Massive MIMO antenna arrays.

INDEX TERMS Antenna array mutual coupling, base station antennas, dual-polarized antennas, partial reflective decoupling layer, dummy decoupling probe, multiple input multiple output (MIMO), 5G.

I. INTRODUCTION

THE 3GPP RAN Plenary has started the standardization of U6G (6425–7125 MHz) as a new IMT-licensed frequency band, and is planned to complete it in the year 2022 [1], following the proposal of U6G bands in the Final Acts of World Radiocommunication Conference 2019 (WRC-19) [2]. This marks a milestone in the industrialization of U6G. In this new band, as the wavelength becomes even smaller than existing commercial 5G bands, the antenna elements and array will become increasingly compact, enabling MIMO antenna arrays to be larger in scale, supporting higher capacity and greater beamforming capability [3]. In the current trend of miniaturization and integration of different communication systems, larger-scale antenna arrays still have to be arranged in a limited volume, therefore, the spacing between antenna elements in a U6G antenna array is also limited as those in Sub-6G bands. There will be strong mutual interaction between adjacent and non-adjacent elements. These coupling effects lead to unacceptable negative impacts, such as distortion of the antenna radiation pattern and reduction of total efficiency, resulting in system-level performance degradation [4]. Therefore, reducing the mutual coupling between antenna elements is an indispensable step for the development of future U6G mobile communications.

Recently, researchers have made significant endeavors and proposed a large number of decoupling methods to suppress the mutual coupling between antennas and antenna arrays.

These decoupling methods can be roughly divided into three categories:

1) Directly suppressing electromagnetic propagation between antennas, such as using split ring resonators (SRR) [5], wave-traps [6], electromagnetic bandgap structures (EBG) [7], [8], [9], defected ground structures (DGS) [10], [11], [12], frequency selective surface (FSS) [13] and baffles [14]. SRR can suppress co-polarization and cross-polarization in dual-polarized antenna arrays. EBG provides a good decoupling solution for surface wave-caused couplings. DGS suppresses surface currents between antennas by etching slots in the ground, which is ineffective for coupling in space and additional backward radiation should be carefully controlled.

2) Utilizing the intrinsic characteristics of antenna elements without adding additional decoupling structures [15], [16], [17]. For example, [15] manipulates the higher order mode to achieve mutual coupling reduction, while [16] uses the induced current from common ground to cancel out the original couplings through radiation.

3) Introducing an intentional coupling path to neutralize the original coupling is also another choice, such as neutralization line (NL) [18], [19], parasitic elements [20], [21], decoupling ground (DG) [22], and decoupling network [23], [24]. Reference [25] achieves high isolation by flexibly controlling the electric and magnetic coupling. In [26], the strong coupling can be suppressed by inserting a lumped element between closely spaced patch antennas. Concerning the concept of phase balance, an accurate design is achieved in [27] by calculating the required phase shift to be generated by the decoupling structure to improve the isolation. In [28], two elements in a subarray are made to form a pair of phase-reversed coupling paths for decoupling. However, most of the researchers have focused on decoupling between a limited number of elements or elements with limited bandwidth, while extending them to multivariate arrays with complex coupling situations requires long-term tuning and optimization. Recently, the idea of using various kinds of metasurface superstrates to create intentional extra reflections to counteract existing coupling is becoming very popular [29], [30], [31], [32], [33], [34], [35], [36], [37], [38]. In [30], the decoupling of only two single-polarized antennas is studied. While [29], [31], [32], [33] and [35], [36], [37], [38] are shown to be effective methods for suppressing the coupling of dual-polarized antenna arrays. Yet in most of the abovementioned designs, the inter-element spacing is not that extreme since at least 0.4 $\lambda 0$ ($\lambda 0$ is the free-space wavelength at the center frequency) minimum clearance from nearby elements is maintained. Whether one can further reduce the array dimension still remains to be a challenging issue, especially for dual-polarized antenna elements.

Based on preliminary works of our group on dual-elements [30] and array [31], [36], [37], this paper investigates a U6G massive MIMO antenna array with a larger scale and closer inter-element spacing. A systematic decoupling method using two layers of PRDL and two types of DDPs is proposed to reduce all types of coupling, especially the co-polarization couplings of adjacent components. PRDL is a thin-layer superstrate of the array, which is usually composed of periodically arranged metal patches to generate a predefined dielectric constant. Two layers of PRDL are sequentially introduced so that the reflected waves are equal in magnitude and opposite in phase to the original coupling waves, suppressing the respective couplings. DDPs are used as auxiliary measures to further reduce the remaining couplings. The ingenious design of both the PRDLs and DDPs can eventually improve the isolation of the whole array.

This paper will consist of the following four parts: Section II will present the decoupling theory and design for a dual-polarized antenna array. Section III shows the evaluation of the key performances of the array. Conclusions will be drawn in Section IV.

II. THEORY AND DESIGN

A. THE ANTENNA ELEMENT AND ARRAY CONFIGURATION

The original 6 × 4 antenna array with power combiners is shown in Fig. 1 (a). The array is arranged in a staggered configuration, which is widely exploited in the FDD (Frequency Division Duplexing) Massive-MIMO system (FMM). The advantage of staggered arrays is the ability to maximize element spacing while maintaining compact arrangement at the subarray level. The array includes 24 dual-polarized elements with $\pm$ 45 $^\circ$ polarization. Every three dual-polarized elements in the vertical direction (along the y-axis in Fig. 1) are combined by two power combiners (one for each polarization) to form a subarray, enhancing realized gain for the feed port. Therefore, there are in total 16 ports. The distance between adjacent horizontal (along the x-axis in Fig. 1) elements in the array is 16 mm (0.36 λ_0, λ_0 is the free-space wavelength at 6.8 GHz), while the distance between vertical elements is 29 mm (0.65 λ_0), which is to prevent the elements from overlapping in the x-axis and maximize the realized gain of the subarray. As can be seen from Fig. 1, this array configuration places stringent constraints on the element size in the first place. The element must be extremely small in size in order to avoid overlapping with each other.

Therefore, a miniaturized dual-polarized quadruple folded dipole (QFD) element proposed by our group [39] is redesigned in the U6G band which is shown in Fig. 2. The radiating component of the antenna element consists of four folded dipoles, four pairs of coplanar strip-lines, and eight downward bending arms, which are all printed on Rogers 4350 substrates with the thickness of 0.254 mm and the dielectric constant of 3.66, as shown in Fig. 2(a) and Fig. 2(b). The two orthogonal polarizations of the antenna element are excited by two printed Marchand balun with slot line feeding structures, which are etched on both sides of a Rogers 4350 substrate with the thickness of 0.508 mm, as shown in Fig. 2(c) and Fig. 2(d) respectively. The downward-bending arm is designed in a meandering

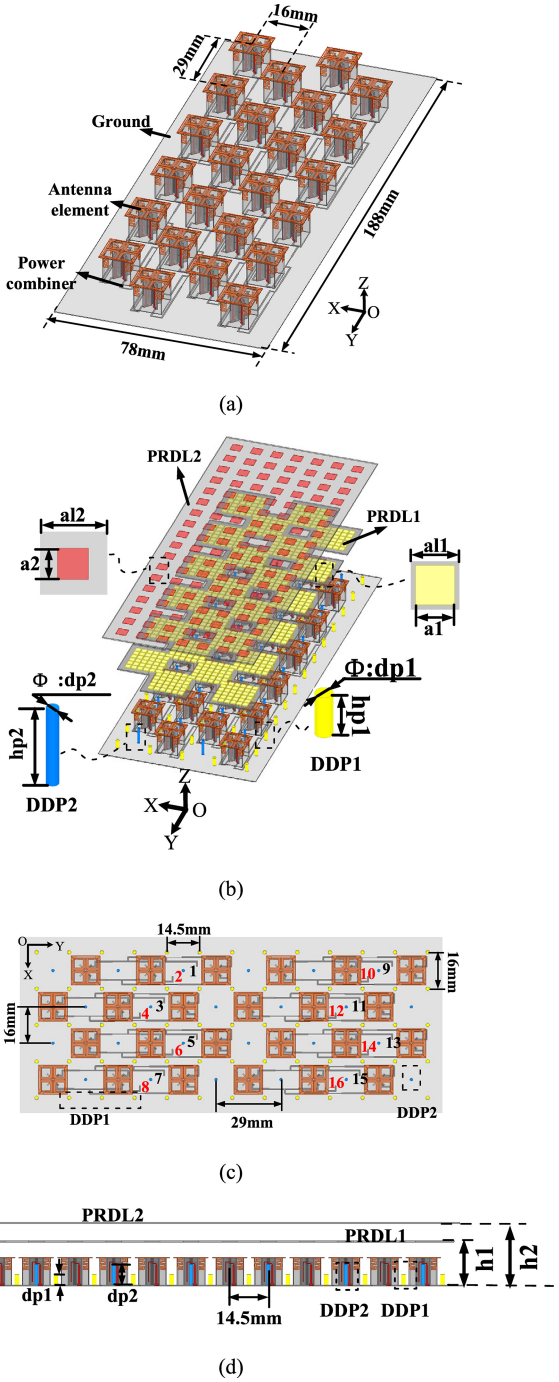

FIGURE 1. (a) Isometric view of the 6 × 4 original antenna array; (b) Explosive view of the 6 × 4 decoupled antenna array; (c) Top view of decoupled antenna array with PRDL hidden (including feed port labels); and (d) Side view of the decoupled array.

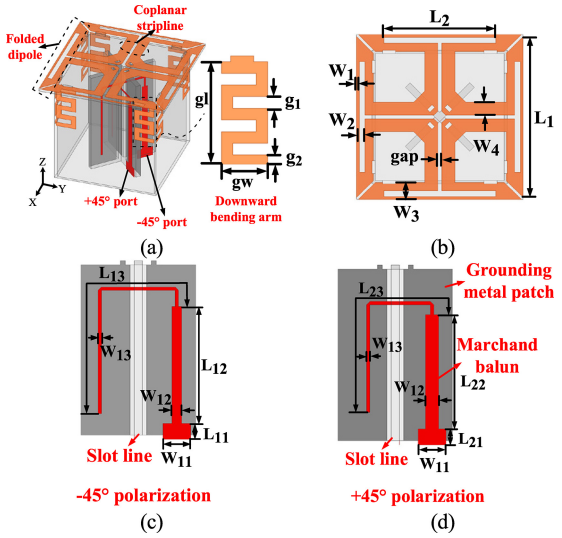

FIGURE 2. Antenna element in (a) 3D view, (b) Top view; (c) feed balun of the −45° polarization and (d) feed balun of the +45° polarization.

TABLE 1. Detail dimensions of antenna element (unit: mm).

Parameters	L_1	L_2	W_1	W_2	W_3	W_4	gap
Value	12.5	8.6	0.2	0.45	1.3	1	0.3
Parameters	L_{11}	W_{11}	L_{12}	W_{12}	L_{13}	W_{13}	L_{21}
Value	0.95	1.7	7.1	0.8	12	0.2	0.95
Parameters	L_{22}	L_{23}	g_l	gw	g_1	g_2	
Value	6.9	10.8	4.4	2	0.5	0.4	

shape to extend the current path and achieve extreme miniaturization. By adjusting the gap g_1 of the downward bending arm, its equivalent capacitance and inductance are optimized to enhance the impedance matching of the miniaturized element. Finally, the element size of $0.29\lambda_0 \times 0.29\ \lambda_0 \times 0.25\ \lambda_0$ is realized, and the detail dimensions are shown in Table 1.

This extreme array configuration and spacing will inevitably cause complex and severe coupling issues, while a single decoupling technique cannot suppress all types of couplings simultaneously. Thus, various measures are needed to cooperate for good decoupling performance.

The decoupling structures designed in this paper include the first PRDL (PRDL1), the second PRDL (PRDL2), the first type of DDP (DDP1) and the second type of DDP (DDP2), as shown in Fig. 1 (b) and Fig. 1 (c). PRDL1 and PRDL2 are suspended above the array one after another, and the distances between them and the common ground of the antenna array are *h1* and *h2* respectively, as shown in Fig. 1 (d). PRDL1 consists of square metal patches with the length of *a1* that are periodically printed on both sides of a Rogers 4350 substrate with the thickness of 0.5 mm. PRDL2 is a superstrate that consists of square metal patches with the length of *a2* periodically printed on only one side of a Rogers 4350 substrate with a thickness of 0.5 mm. Totally 65 DDP1s are placed at the four corners of every element, and the separation between DDP1s along the *x*- and *y*-axis are 16mm and 14.5mm respectively. DDP2 is placed in the middle of the two vertically arranged elements, which are 24 in total, and the distance of DDP2 in the x and y-axis are 16 mm and 29 mm, respectively. The power combiners are printed on the bottom of a Rogers 4350 substrate with a thickness of 0.254 mm, the ground is printed on the top side, upon which all antenna elements and decoupling structures are placed, as shown in Fig. 1 (b) and (c). The dimensions related to the 6 × 4 decoupled array are shown in Table 2.

TABLE 2. Detail dimensions of 6 × 4 decoupled antenna array (unit: mm).

Parameters	dp1	dp2	a1	h1	hp1	hp2
Value	1.6	1.2	2.56	17	4	8
Parameters	a2	h2	al1	al2		
Value	5.4	24	3	10		

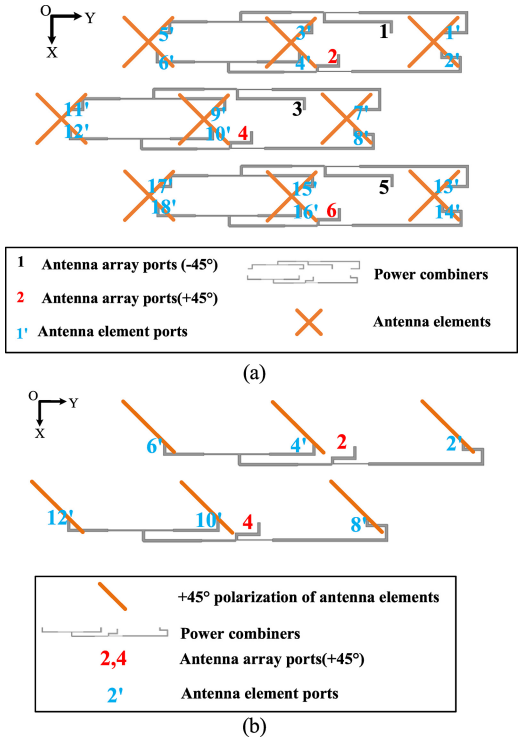

FIGURE 3. Schematic of the partial port arrangement of the 6 × 4 coupled array (Top View). (a) Arrangement of ports 1-6. (b) Arrangement of adjacent columns with the same polarization (+45°).

B. COUPLING ANALYSIS OF ELEMENTS AND SUBARRAY WITH POWER COMBINERS

With the introduction of the power combiner, various kinds of element couplings are mixed, making the situation more complex. With the help of network analysis and scattering parameter calculation, it can be concluded that the port coupling after the introduction of the power combiner can be superimposed from the couplings between antenna elements under certain circumstances (Due to the phase shift of the power combiner itself, this paper only discusses the magnitude for reference).

Take a subarray shown in Fig. 3 (a) for instance, since the co-polarization couplings (S_{13}, S_{24}, S_{35} and S_{46}) of adjacent columns are stronger in most cases, the coupling between ports 2 and 4 is taken here as an example to study the coupling combining effect, as shown in Fig. 3 (b). From network point of view, $|S_{24}|$ can be expressed as:

$$|S_{24}| \approx (|S_{2'8'}| + |S_{4'10'}| + |S_{6'12'}| + |S_{4'8'}| + |S_{6'10'}| + |S_{2'10'}| + |S_{2'12'}| + |S_{4'12'} + |S_{6'8'})|/3 \quad (1)$$

where $|S_{ij}|$ stands for the magnitude of couplings with power combiners between subarray port i and subarray port j, the primed symbols $|S_{i'j'}|$ stands for the magnitude of couplings between element port i' and element port j'. It should be noted that minor couplings from distant elements and subarrays are omitted in equation (1) to shed light on the key factors (i.e., the major couplings).

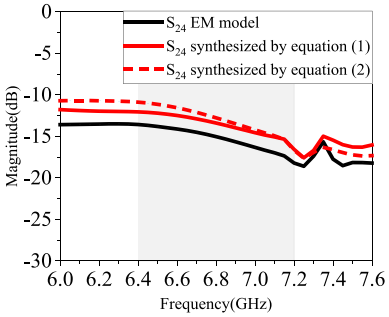

FIGURE 4. The magnitude of S24 from simulation and calculation.

The magnitude plots of S_{24} using the power combination relation in equation (1) are given in Fig. 4 (the red solid line). It can be observed that it has a consistent trend in magnitude compared to the direct simulated S_{24} of the electromagnetic (EM) model while the power combiner is present (the black solid line). There are 2-3 dB discrepancies between magnitude, due to the ideal equal power combining assumption in (1).

For the two adjacent elements between two different columns/subarrays, the E-plane co-polarization coupling (such as $S_{4'8'}$) and the H-plane co-polarization coupling (such as $S_{2'8'}$) are the strongest couplings and the key couplings to be dealt with. Ignoring other minor couplings in equation (1), the coupling between ports 2 and 4 can be composed of five major couplings as follows:

$$|S_{24}| \approx (|S_{2'8'}| + |S_{4'10'}| + |S_{6'12'}| + |S_{4'8'}| + |S_{6'10'}|)/3 \quad (2)$$

It contains 3 H-plane couplings ($S_{2'8'}$, $S_{4'10'}$ and $S_{6'12'}$) and 2 E-plane couplings ($S_{4'8'}$ and $S_{6'10'}$) between the elements. It is known from Fig. 4 that the curve calculated by equations (2) and (1) are in good agreement, proving that the simplification from (1) to (2) is valid. From (2), it is obvious that if the two major couplings between elements are well under control, the isolation magnitude between subarrays can also be effectively reduced.

C. PRDL DECOUPLING MECHANISM

To better study the decoupling mechanism, two typical antenna elements in the array are taken for further analysis, as shown in Fig. 5, which are two adjacent elements from two adjacent subarrays. Two PRDLs are placed one after another as the superstrates of the two antenna elements, as shown in Fig. 6. PRDL1 introduces the reflected wave ③ to neutralize the original coupled wave ① + ②, where ① stands for space wave coupling and ② stands for coupling from ground reflection with phase reversal. Then, one can treat the antenna elements and the PRDL1 as a whole new structure. The

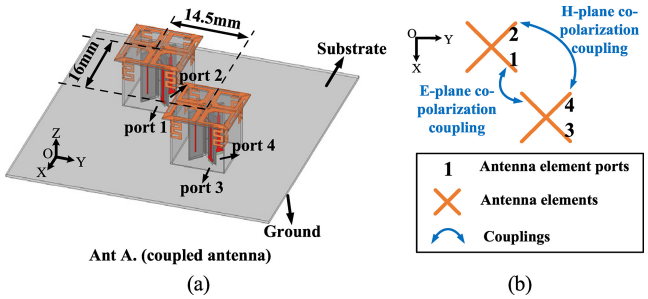

FIGURE 5. Isometric view of 2-element antenna model without any decoupling measures. (a) 3D view. (b) Antenna configuration and coupling condition (Top view).

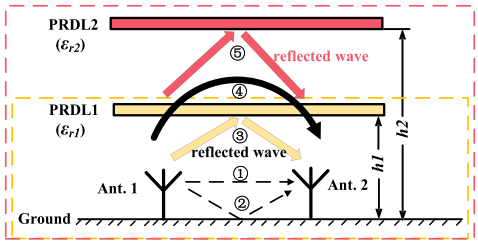

FIGURE 6. Illustration of a 2-element dual-polarized antenna pair with two PRDLs (Direct coupling between elements ①, indirect coupling reflected by the ground ②, reflected wave introduced by PRDL1 ③, coupling wave between elements after loading PRDL1 ④, reflected wave introduced by PRDL2 ⑤).

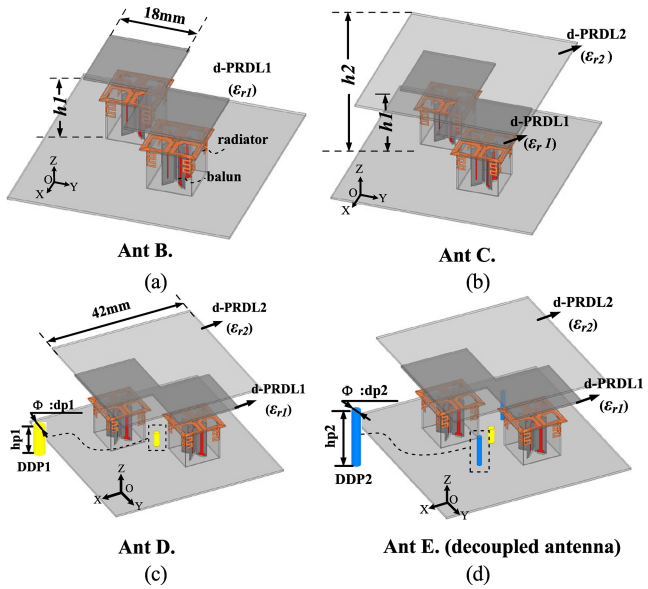

FIGURE 7. Isometric view of 2-element antenna model (a) Load d-PRDL1. (b) Load d-PRDL1 and d-PRDL2. (c) Load d-PRDL1, d-PRDL2 and DDP1. (d) Load d-PRDL1, d-PRDL2, DDP1 and DDP2.

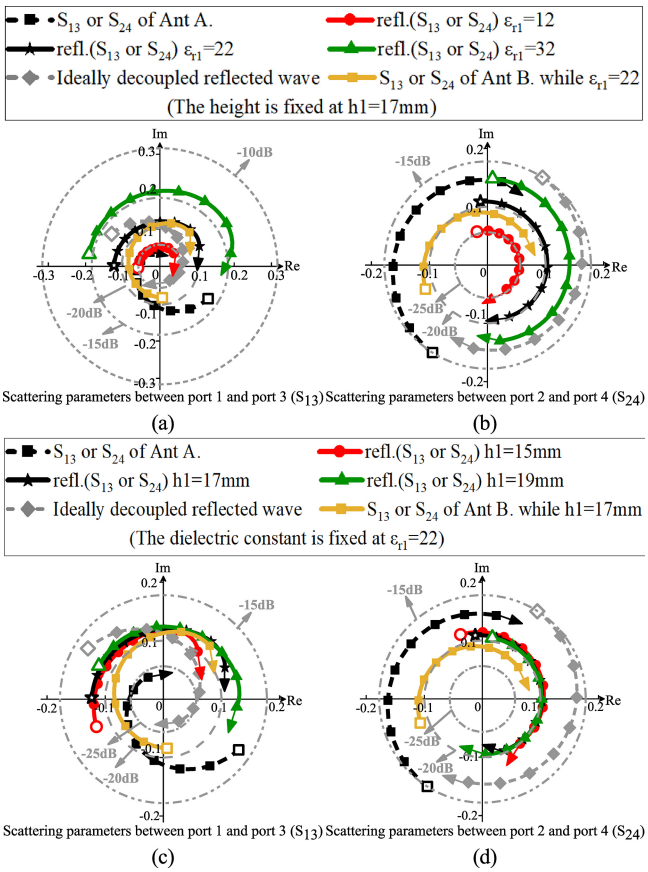

FIGURE 8. Polar plot showing the influence of d-PRDL1 on a reflected wave of the 2-element antenna. ε_{r1}'s influence on (a) refl. (S_{13}), (b) refl. (S_{24}). h1's influence on (c) refl. (S_{13}), (d) refl. (S_{24}). (refl. (S_{13}) represents the reflected wave between port 1 and port 3 introduced by the d-PRDL1 and refl. (S_{24}) represents the reflected wave of port 2 and port 4 introduced by d-PRDL1).

remaining coupling after the introduction of RRDL1 is marked as ④. To cancel that remaining coupling, PRDL2 is then introduced to generate a new reflected wave ⑤. The dielectric constant and height of PRDL2 are carefully designed to be equal in magnitude and opposite in phase to ④ to achieve better decoupling performance. Furthermore, since PRDL is in fact an artificial dielectric material. In order to save computational resources, dielectric PRDL (d-PRDL, a dielectric board with a prescribed dielectric constant) is used instead of PRDL in the following study, as shown in Fig. 7.

The analysis of the relation between the original couplings of respective antenna polarizations and the couplings introduced by PRDL is conducted by S-parameters in polar plots, as shown in Fig. 8. The hollow markers of every curve represent the start frequency which is 6.4 GHz in this example. The solid arrows of every curve show the stop frequency, which is 7.2 GHz while the step frequency is 0.1 GHz, shown by the solid markers on the curve. In order to also reveal the decibel magnitude of the respective couplings, which is more commonly used in practice, several concentric circles are used to indicate different levels of isolations in decibels. The magnitude and phase of the concerned couplings at each frequency point can be well identified in the polar plot, and the decibel magnitude of isolation can also be identified with the help of decibel reference circles, where the ideally reflected wave to cancel the original coupling wave is also plotted for reference, as marked by the gray dash line in Fig. 8.

d-PRDL1 with height *h1* and dielectric constant ε_{r1} is loaded above Ant A. (Fig. 5a) to form Ant B., as shown in

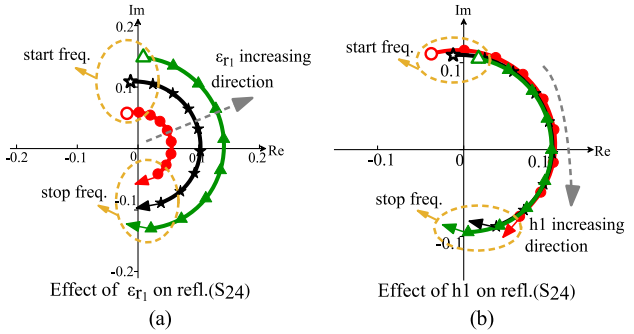

FIGURE 9. Effect of (a) ε_{r1}, (b) h1 of d-PRDL1 on the reflected wave refl. (S24) of the 2-element antenna.

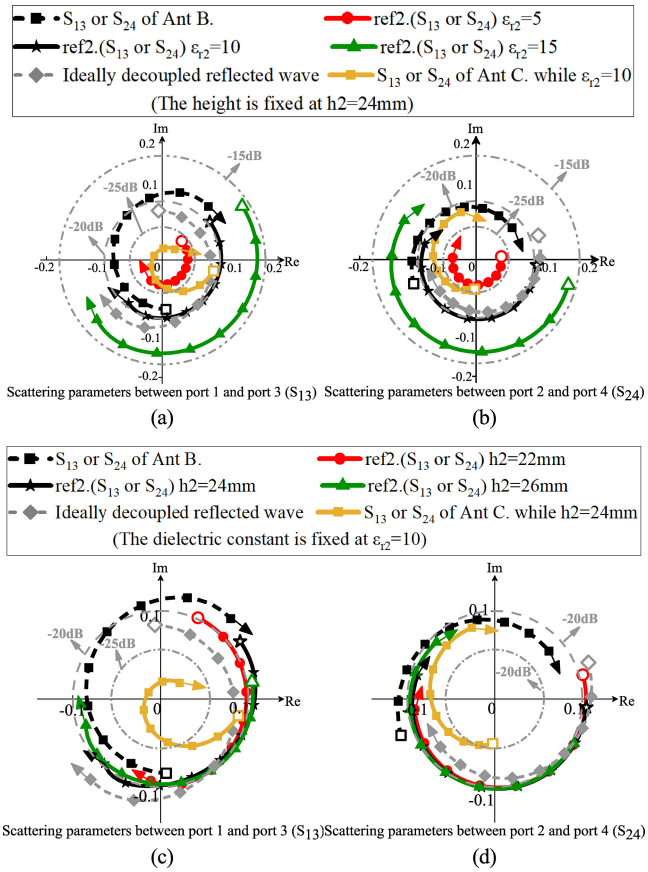

FIGURE 10. Polar plot showing the influence of d-PRDL2 on a reflected wave of the 2-element antenna. ε_{r2}'s influence on (a) ref2.(S_{13}), (b) ref2.(S_{24}). h2's influence on (c) ref2.(S_{13}), (d) ref2.(S_{24}). (ref2.(S_{13}) represents the reflected wave between port 1 and port 3 introduced by the d-PRDL2 and ref2.(S_{24}) represents the reflected wave of port 2 and port 4 introduced by d-PRDL2).

Fig. 7 (a). The square dielectric plate with the side length of 18 mm is placed separately above the antenna instead of using a whole d-PRDL1, which can reduce the propagation of the transverse electric field and improve the cross-polarization discrimination [30]. Fig. 8 shows the polar plot of the original couplings of Ant A. and the reflected waves introduced by the d-PRDL1 with different height *h1* and dielectric constant ε_{r1} in Ant B. The two major couplings, E-plane mutual coupling S_{13} and H-plane mutual coupling S_{24} are shown and investigated, while refl.(S_{13}) represents the reflected wave between port 1 and port 3 introduced by the d-PRDL1 and refl. (S_{24}) represents the reflected wave between port 2 and port 4 introduced by d-PRDL1 concerning different dielectric constants and heights. Fig. 9 shows the trend of a reflected wave when ε_{r1} and *h1* vary (taking refl.(S_{24}) as an example). It can be concluded from Fig. 8 and 9 that:

1) The dielectric constant of d-PRDL1 controls the magnitude of the reflected wave. With the increase of ε_{r1}, the magnitude of the reflected wave increases accordingly. When the value of ε_{r1} changes from 12 to 22, the magnitudes of refl. (S_{13}) and refl. (S_{24}) range from 0.05 to 0.12 and 0.05 to 0.1, respectively. For ports 1 and 3, the magnitude of ideally decoupled reflected wave (gray dash line in Fig. 8 (a)) required for 6.4 GHz and 7.2 GHz is 0.13 and 0.02 respectively, which is clearly frequency dependent. For ports 2 and 4, it is clear that $\varepsilon_{r1} = 32$ will result in an almost ideal decoupling condition, but if the reflected wave is too large, it will deteriorate the matching performance as well as the decoupling condition of S_{13} in Fig. 8 (a). After comprehensive consideration, $\varepsilon_{r1} = 22$ is selected at this stage. The above analysis also demonstrates that it is not possible to use only one PRDL to eliminate the two major couplings.

2) The height of d-PRDL1 mainly affects the phase of the reflected waves and has almost no effect on the magnitude, this is understandable since the phase difference is equivalent to the path difference from the PRDL to the antenna aperture. With the increase of *h1*, the curve of the reflected wave rotates clockwise along the concentric circle, as shown in Fig. 9 (b). Nevertheless, it can be seen from Fig. 8 (c) and (d) that one cannot find a proper *h1* so that the d-PRDL1 can decouple both S_{13} and S_{24} simultaneously and perfectly.

The optimum results (yellow line) after adding d-PRDL1 are also superposed in Fig. 8, where S_{24} is reduced from −15dB to −20 dB, and the magnitude difference between the reflected wave and the ideally decoupled reflected wave is 0.05, and the phase difference is about 30°, which does not reach the optimal decoupling state. While S_{13} deteriorates from –25dB to –18 dB at 7.2 GHz, the difference in magnitude between the reflected wave and the ideally decoupled reflected wave is 0.07, and the phase difference is 80°, which is far from the perfect decoupled phase. It should be mentioned that the thickness of the PRDL will also affect mainly the magnitude of the reflected waves, but due to the limited choice of available thickness of PCBs in practice, this variable is kept to be a fixed one in this paper.

Therefore, it is necessary to introduce the second layer of d-PRDL (d-PRDL2) above d-PRDL1, as shown in Ant C. of Fig. 7 (b). Taking Ant B. as a whole new antenna system, the introduction of d-PRDL2 generates a new reflected wave ⑤ between elements (as shown in Fig. 6). Fig. 10 shows the polar plot of the coupling waves of Ant C. and the

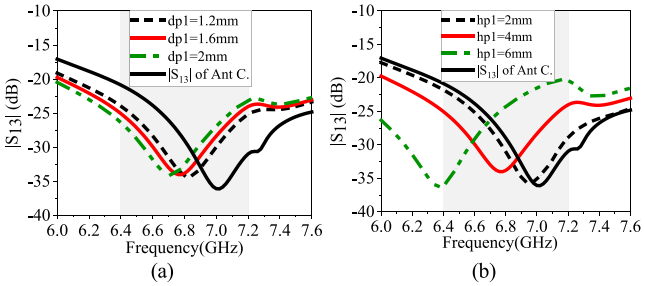

FIGURE 11. Influence of DDP1 structural parameters to Ant D. on S_{13}. (a) dp1. (b) hp1.

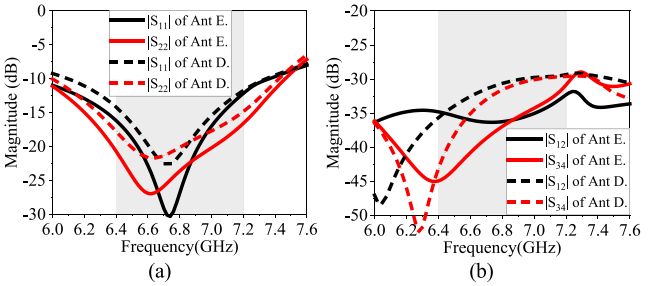

FIGURE 12. Comparison of (a) S_{11} and S_{22}, (b) S_{12} and S_{34} before and after adding DDP2 to the 2-element antenna forming Ant E.

reflected waves introduced by the d-PRDL2 with different height *h2* and dielectric constant ε_{r2}. The effect of d-PRDL2 on Ant B. is similar to that of d-PRDL1 as summarized previously. The introduction of d-PRDL2 compensates for the magnitude difference between refl.(S_{24}) and the ideally decoupled reflected wave. The increase in its height brings an additional reflection phase that compensates for the phase of refl.(S_{13}) at 7.2 GHz. When $\varepsilon_{r2} = 10$ and $h2 = 24$ mm, a compromise between matching and decoupling is attained. For H-plane coupling S_{24}, the reflected wave introduced by d-PRDL2 can achieve good coupling cancellation, and S_{24} is reduced to –22 dB in the operating band. For E-plane coupling S_{13}, at 7.2 GHz, the coupling is reduced by 12 dB, but at 6.4 GHz, the magnitude difference between ref2. (S_{13}) and the ideally decoupled reflected wave is 0.02, and the phase difference is 60°. There is still a need for further decoupling measures.

D. ADDITIONAL DECOUPLING DESIGN USING DDPS

DDP1 is placed between the two corners of the elements, as shown in Fig. 7 (c) (Ant D.), with the height of *hp1* and the diameter of *dp1*. DDP1 mainly affects E-plane coupling (S_{13}). When port 2 of Ant D. is excited, DDP1 is in the region where the field induced is weak, so its effect on H-plane mutual coupling is neglectable. The decoupling effect of S_{13} with the variation of the structural parameters of DDP1 is given in Fig. 11. It can be observed that DDP1 is able to move the decoupling band notch of Ant D. to a lower frequency. When *hp1* = 2 mm and *dp1* = 1.6 mm, the nadir of S_{13} moves from 7 GHz to 6.7 GHz, dropping below –25 dB in the operating band. Compared with *dp1*, S_{13} is more sensitive to *hp1*.

The DDP2 with height *hp2* and diameter *dp2* is placed in the position shown in Fig. 7 (d) (Ant E.). The introduction of DDP2 improves the port matching while suppressing the coupling between the two ports of every element, as shown in Fig. 12.

Ant A-E. give a complete decoupling design guideline. By properly designing d-PRDLs and DDPs and optimizing their design dimensions, the S_{13} and S_{24} can be reduced to below −22dB in the frequency band of interest while ensuring good matching.

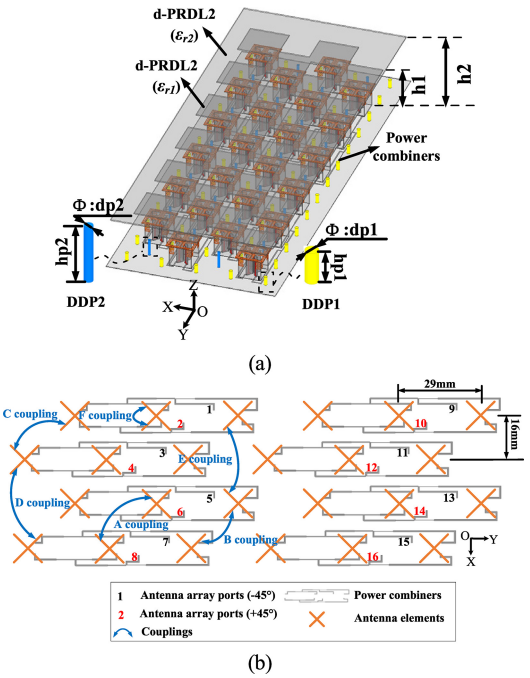

FIGURE 13. (a) 3D view of the 6 × 4 decoupled array with d-PRDL. $\varepsilon_{r1} = 22$, $\varepsilon_{r2} = 10$. (b) Coupling classification of 6 × 4 array.

E. APPLYING THE DECOUPLING MEASURES TO THE 6 × 4 ARRAY

A final 6 × 4 array can be formed by periodically replicating Ant E. while introducing 8 pairs of three-way power combiners, as shown in Fig. 13 (a). To facilitate the discussion of decoupling results, the couplings of the antenna array are divided into six categories A-F, as shown in Fig. 13 (b). There is a high level of isolation between two 3 × 4 subarray ports (e.g., Port 1 and Port 9), and the discussion is omitted. Due to the symmetry of the array, only the S-parameters of ports 1-8 are studied in detail:

A-couplings (S_{24}, S_{35}, S_{68}): co-polarization couplings in the H-plane between adjacent columns of subarrays;

B-couplings (S_{13}, S_{46}, S_{57}): co-polarization couplings in the E-plane between adjacent columns of subarrays;

C-couplings (S_{14}, S_{23}, S_{36}, S_{45}, S_{58}, S_{67}): cross-polarization couplings between adjacent columns of subarrays;

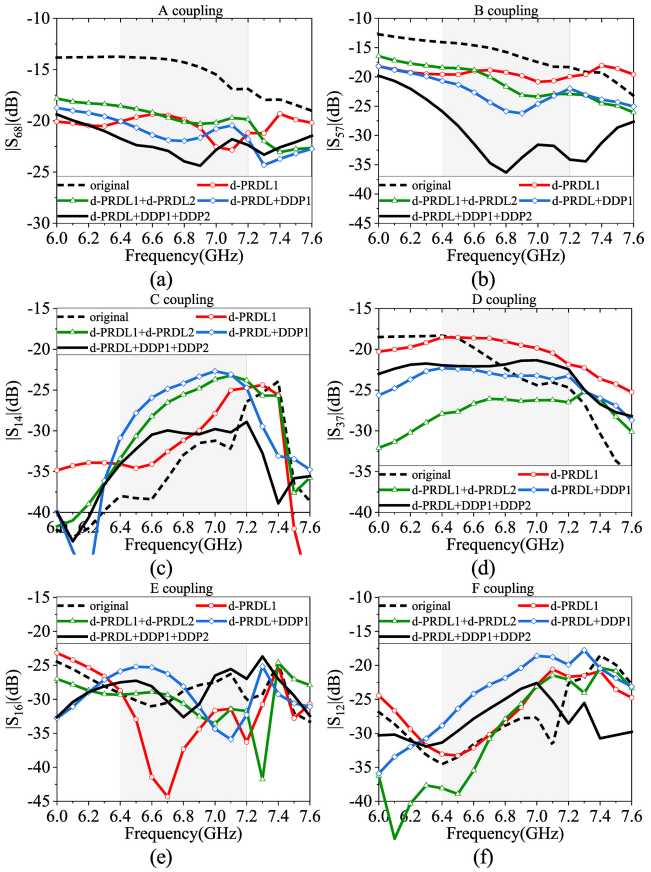

FIGURE 14. Simulated mutual couplings with different decoupling measures of 6 × 4 array. (a) A coupling(S_{68}), (b) B coupling(S_{57}), (c) C coupling(S_{14}), (d) D coupling(S_{37}), (e) E coupling(S_{16}), (f) B coupling(S_{12}).

D-couplings (S_{15}, S_{26}, S_{37}, S_{48}): co-polarization couplings between two nonadjacent columns of subarrays;

E-couplings (S_{16}, S_{25}, S_{38}, S_{47}): cross-polarization coupling between two nonadjacent columns of subarrays;

F-couplings (S_{12}, S_{34}, S_{56}, S_{78}): cross-polarization coupling between two ports of every column.

Both A and B are co-polarized couplings in adjacent columns. The difference is that A coupling consists mainly of 3 H-plane couplings and 2 E-plane couplings between elements, while B coupling consists mainly of 2 E-plane couplings and 3 H-plane couplings between elements, as is already discussed in Section II-B.

Fig. 14 gives the variation of the coupling A-F for different decoupling method combinations of the 6 × 4 antenna array. It can be observed from Fig. 14 that A and B are the worst couplings of the array and are the critical couplings to be dealt with.

With the introduction of d-PRDL1, the A coupling is reduced by about 4-6 dB over the bandwidth, and the polar plot about the reflected wave of A coupling introduced by d-PRDL1 is given in Fig. 15 (a). It is observed that there is a difference of 0.08 in magnitude and 15° in phase with the ideally decoupled reflected wave at 6.4 GHz, while at 7.2 GHz, the difference in magnitude is 0.01 and the

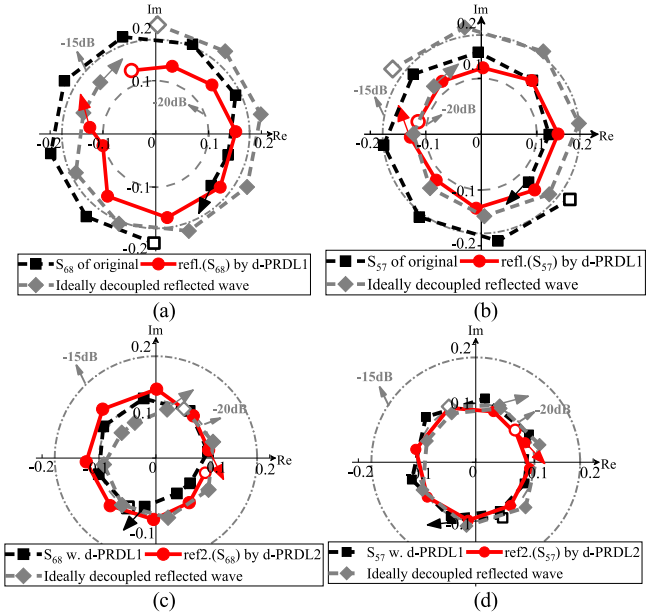

FIGURE 15. Polar plot showing the influence of d-PRDL1 on (a) A coupling, (b) B coupling; Polar plot showing the influence of d-PRDL2 on (c) A coupling, (d) B coupling.

phase difference is 40°. The B coupling is reduced by about 2-5 dB in the operating band. Fig. 15 (b) gives the polar plot about the reflected wave of B coupling introduced by d-PRDL1, which is in a similar pattern with the A coupling reflected wave, where the magnitude difference is large at lower frequencies and the phase difference is large at higher frequencies. With the introduction of the power combiner, the A and B couplings combine the characteristics of the E-plane and H-plane couplings between the elements, which means that the d-PRDL1 alone cannot solve the A and B couplings perfectly. d-PRDL1 simultaneously reduces the E coupling but has a destructive effect on the C, D and F couplings. Nevertheless, this is only an intermediate process. Both C and F couplings are < -20 dB in the presence of d-PRDL1, and D coupling tends to be flatter over the whole frequency band.

The d-PRDL2 reduces the B coupling at high frequencies, as shown in Fig. 14 (b). Fig. 15 (c) and (d) give the polar plot of the reflected waves introduced by d-PRDL2 regarding the A and B couplings. The phase difference between the A coupling at 6.4 GHz and 7.2 GHz with the ideally decoupled reflected wave is 80° and 70° respectively, which is far from the decoupling phase condition, so the coupling becomes stronger. It is also clear from the figure that the proposed d-PRDL2 mainly compensates for the magnitude of the reflected wave, making it closer to the magnitude of the ideally decoupled reflected wave, shown in the gray lines in Fig. 15 (c) and (d). But the phase difference between them becomes larger. Therefore, the optimum decoupling result is not achieved. The C and E coupling deteriorates with the introduction of d-PRDL2, but remains at below –25 dB, while there is almost no effect on the F coupling.

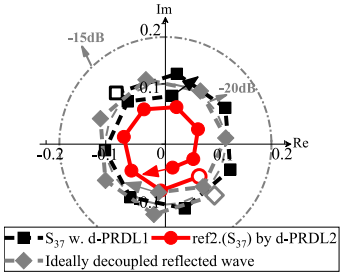

FIGURE 16. Polar plot showing the influence of d-PRDL2 on D coupling (ref2. (S_{37})).

DDP1 is added at the four corners of the element to achieve further coupling suppression by optimizing its height. DDP1 can adjust the E-plane coupling operating band between the elements. As can be seen in Fig. 14 (a) and (b), the introduction of DDP1 results in a reduction of the A and B couplings by about 2 dB at low frequencies. DDP1 does not affect C and E couplings. DDP1 affects the electric field near the subarray and the F-coupling is disrupted, rising to −18 dB. In the array, between the D coupling reflected wave introduced by d-PRDL2 and the original coupling wave is almost zero, as shown in Fig. 16, while the presence of DDP1 introduces an additional path difference that destroys the phase balance of the D coupling, so it deteriorates to −22 dB, but this can be accepted.

DDP2 is another metal structure with a different height and position compared with DDP1, located around the elements and in the middle of the different polarization power combiners of the columns, i.e., the blue circular structure in Fig. 1 (c). They block the propagation of partially coupled waves and can suppress F coupling. At the same time, the A and B coupling can be further suppressed, and the B coupling has a 10 dB reduction at 6.8 GHz. There is almost no effect on the D and E couplings. It mainly suppresses the cross-polarization coupling of adjacent subarrays (C coupling) to keep it below −30 dB, as shown in Fig. 14 (c).

To visualize the decoupling mechanism of the proposed structure, Fig. 17 shows the electric field distribution of the array at 6.8 GHz when port 5 or port 6 is excited, with the sequential addition of d-PRDLs and DDPs. It can be observed that when there are no decoupling structures, a strong coupling electric field is induced on the adjacent subarrays. After loading the d-PRDLs, the coupled electric field on the adjacent sub-array is significantly weakened when port 5 is excited, as shown in the left figure of Fig. 17 (b). When port 6 is excited, the introduction of the DDPs further suppresses the coupling electric field and achieves the decoupling of the array, as shown in the right figure of Fig. 17 (c). The above analysis shows that the proposed systematic decoupling structure can effectively reduce the strong co-polarization couplings in the antenna array, while the other couplings remain at a low level.

The d-PRDL is in essence a high dielectric constant substrate, which can definitely be realized in ceramics [30]. Yet ceramics with the certain prescribed dielectric constant

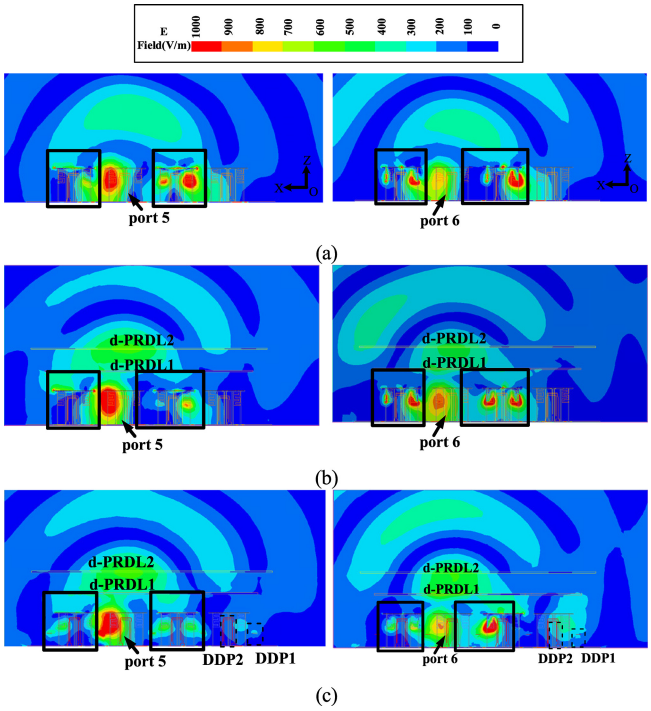

FIGURE 17. Electric field distribution at 6.8 GHz for the 6 × 4 array in the xoz plane when port 5 (left) or port 6 (right) is excited. (a) Coupled array, (b) Array Loading d-PRDLs, (c) Array Loading d-PRDLs and DDPs.

need to be customized for practical applications, which are expensive and require a long processing time. Therefore, the d-PRDLs in Fig. 13 (a) are replaced by PRDLs in Fig. 1 (b) using the equivalence method proposed in [40].

Both PRDL and d-PRDL are in the same location above the array. PRDL1 consists of double-sided metal square patches with side length $a1$, printed on the top and bottom side of a Rogers 4350 substrate with a thickness of 0.5 mm (metal patches are printed on both sides of the substrate to ensure the realization of periodicity of metal square patches printed on the small dielectric board with 18 mm side length). The low loss of this substrate will help to maintain the good efficiency of the antenna array. Since the designed dielectric constant is smaller for PRDL2, it only consists of single-sided metal squares with side length $a2$, which are printed on the top side of a Rogers 4350 substrate with a thickness of 0.5 mm. Both PRDL1 and PRDL2 have periodic properties. The equivalent dielectric constant of PRDL can be calculated by the method in [40].

To obtain the equivalent permittivity of the PRDL, its periodic cell is simulated as shown in Fig. 18, where only the real part of the permittivity that plays a dominant role is shown. From this, it can be seen that the extracted equivalent dielectric constant of PRDL increases with the growth of the edge length of the metal patch. When using a double-layer metal patch ($\varepsilon_{r1} = 22$), the permittivity is more sensitive to the change in size. The final extracted equivalent dielectric constants of PRDL1 and PRDL2 are 22 and 10, respectively, as illustrated by the red solid line in Fig. 18. Fig. 19 shows

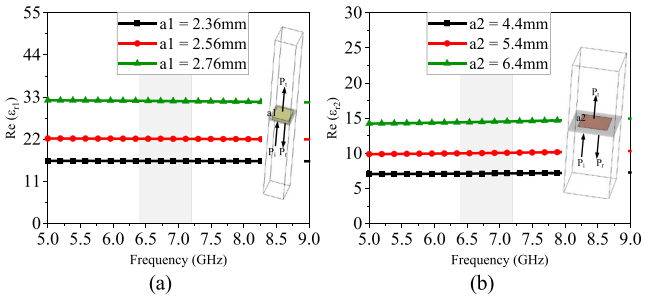

FIGURE 18. (a) Equivalent permittivity extraction for PRDL1 cells at different a1. (b) Equivalent permittivity extraction for PRDL2 cells at different a2.

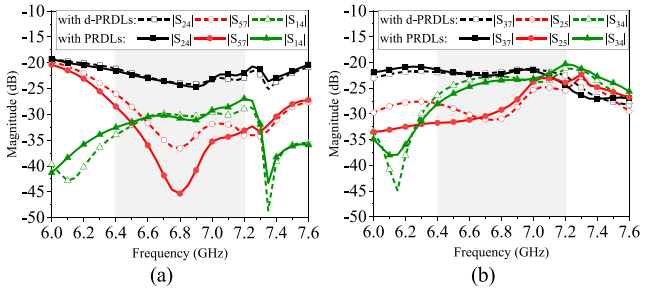

FIGURE 19. Comparison of S-parameters in 6 × 4 decoupled antenna array after loading d-PRDL and PRDL respectively. (a) S_{24}, S_{57}, S_{14}, (b) S_{37}, S_{25}, S_{34}.

the S-parameters of some typical port simulations before and after the equivalent replacement of PRDLs. It can be concluded that the decoupling performance of PRDL and d-PRDL for the antenna array is almost the same. As the permittivity of PRDL is not strictly equal to that of d-PRDL in the operating band and considering the finite number of cells in the PRDL, there are slight differences in the S-parameters of some ports, but the overall trend is comparable. In summary, d-PRDL and PRDL share the same properties and can be substituted for each other. One can first use d-PRDL in the design process to speed up the simulation and then replace it with PRDL consisting of periodic unit cells.

III. ANTENNA ARRAY PERFORMANCE ANALYSIS

To verify the above proposed systematic decoupling method, the compact 6 × 4 dual-polarized QFD array operating in the 6.4-7.2 GHz band is fabricated. The antenna prototype and measurement environment are shown in Fig. 20. Since the designed antenna array works at the U6G band, the fabrication of the prototype needs extra attention on process and tolerance. The radiating part of the antenna element is printed on pieces of PCBs and then they are assembled and soldered. DDPs are small in size and require special customization by adding a 0.5 mm diameter metal cylinder at the bottom to fix them on the ground, as shown in Fig. 21 (a).

Therefore, the finished DDPs are in a stepped cylindrical shape. Due to the close spacing of the array, the power combiners are designed in a meander shape to reduce their footprint, which are printed on the bottom of the Rogers 4350 substrate with thickness of 0.254 mm and a whole

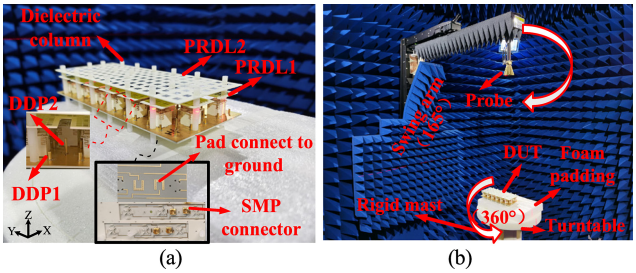

FIGURE 20. Photos of (a) the antenna prototype and (b) the anechoic chamber measuring device.

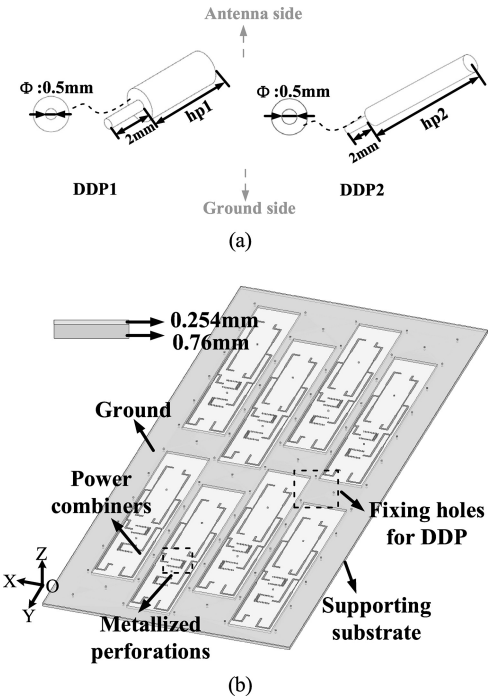

FIGURE 21. Processing and assembling details of (a) DDPs, and (b) Ground layout and supporting structures.

ground layer is printed on the top of the same substrate. A supporting substrate of 0.76 mm thickness and Rogers 4350 material is added under power combiners to support the whole antenna array, which is fixed with nylon poles. The support substrate uses a skeleton form where there are power dividers, as shown in Fig. 21 (b). The support substrate can support the antenna array without affecting the port matching. In the sub-6GHz band, SMA RF connectors are usually used. For this design, the size of the SMA RF connector is too large to be used. Therefore, a suitable SMP connector is selected. The occupied areas of the SMP connectors should be considered in the PCB layout as shown in Fig. 21 (b).

Then measurements are performed on the antenna prototype for performance verification. When measuring the radiation patterns and S-parameters, the other unmeasured antenna ports are connected to 50 Ω loads. The simulated and measured port reflection coefficients of the array are superposed in Fig. 22. After applying the decoupling

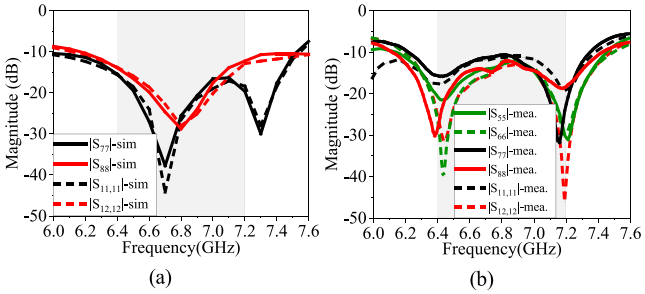

FIGURE 22. Reflection coefficients of selected ports, (a) Simulated results; and (b) Measured results.

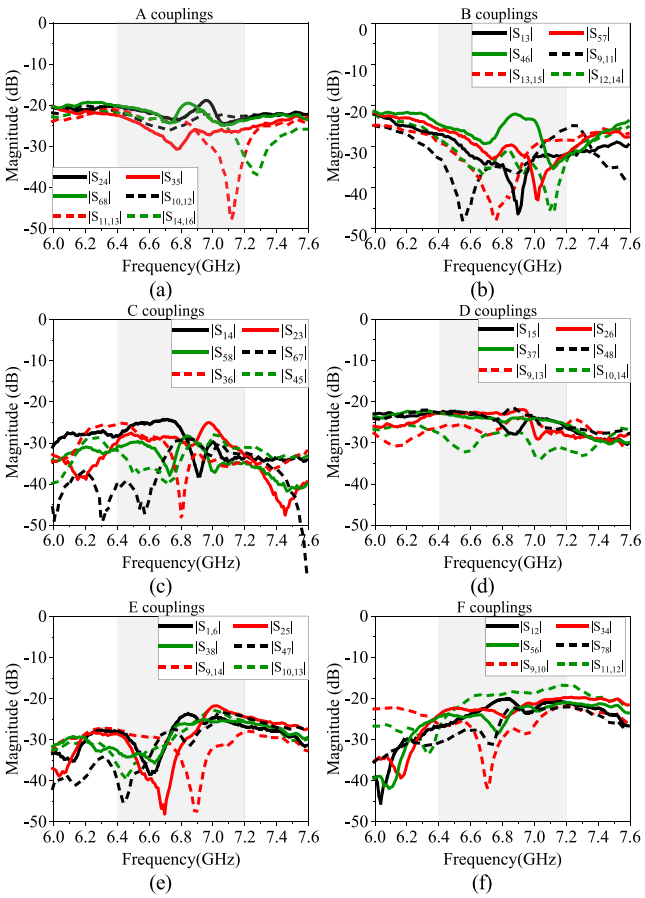

FIGURE 23. Measured S-parameters of the proposed 6×4 array. (a) A couplings, (b) B couplings, (c) C couplings, (d) D couplings, (e) E couplings, (f) F couplings.

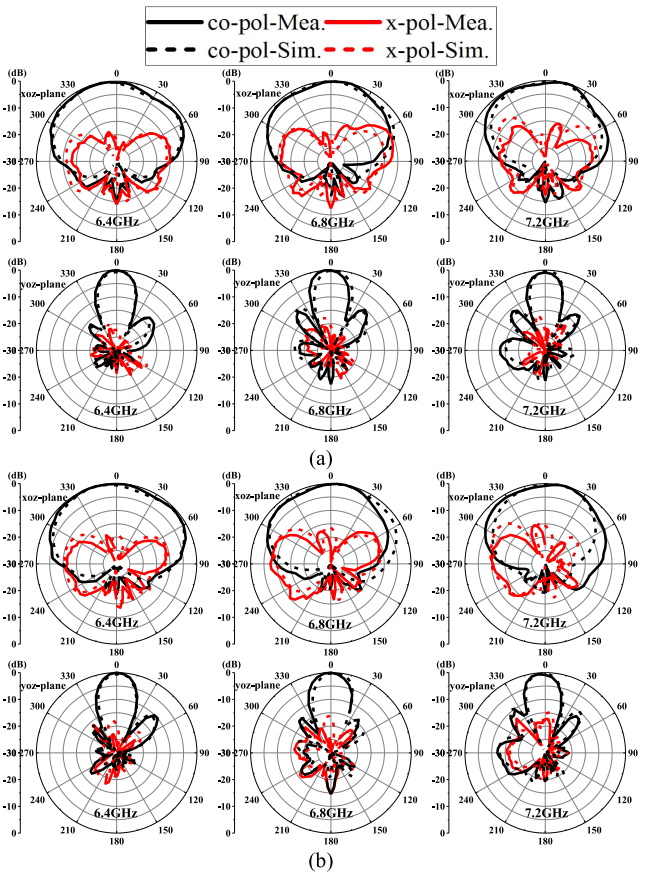

FIGURE 24. Simulated and measured radiation patterns at 6.4 GHz, 6.8 GHz and 7.2 GHz. (a) port 3 is excited. (b) port 4 is excited.

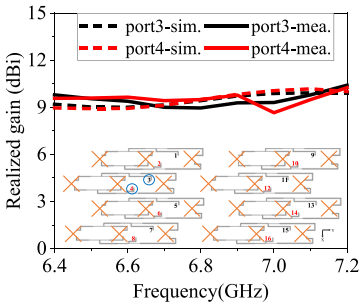

FIGURE 25. Simulated gain before decoupling and simulated and measured realized gain after decoupling when port 3 or port 4 is excited.

measures, the reflection coefficient of the antenna is reduced to −12dB. The measured reflection coefficient of each port has good agreement with each other. Due to the high operating band of the antenna and the complex assembly process, there are slight differences with the ideal model of the simulation, resulting in some differences between the measured and simulated data. Fig. 23 shows the measured data for all coupling of the array in the range of 6.4-7.2 GHz. All couplings are suppressed below −21 dB in the operating band. The effectiveness of the systematic decoupling structure of PRDLs and DDPs on the mutual coupling suppression of the large-scale antenna array is demonstrated.

The antenna radiation pattern is an important figure of merit of antenna performance. In the actual measurement, ports 3 and 4 are selected as representatives to measure their radiation patterns. Fig. 24 gives the simulation and measurement results of the radiation patterns at three typical frequencies when port 3 or port 4 is excited separately after applying the decoupling measures. The simulated and measured realized gains for port 3 and port 4 are shown in Fig. 25, with the realized gain of the subarray remaining at 10 ± 0.5 dBi. It is obvious that the measurement and simulation data are in good agreement.

As one of the key representations of system performance, the envelope correlation coefficient (ECC) of a massive MIMO antenna array should be low enough even for a narrow-angle spread. When the array ECC increases, the channel capacity will eventually deteriorate. The ECC can be calculated by the following equation:

$$\rho_e = \frac{\left|\iint_{4\pi}\left(XPD\cdot E_{\theta i}(\Omega)\cdot E^*_{\theta j}(\Omega)\cdot p_\theta(\Omega)+E_{\phi i}(\Omega)\cdot E^*_{\phi j}(\Omega)\cdot p_\phi(\Omega)\right)d\Omega\right|^2}{\iint_{4\pi}\left(XPD\cdot G_{\theta i}(\Omega)\cdot p_\theta(\Omega)+G_{\phi i}(\Omega)\cdot p_\phi(\Omega)\right)d\Omega \cdot \iint_{4\pi}\left(XPD\cdot G_{\theta j}(\Omega)\cdot p_\theta(\Omega)+G_{\phi j}(\Omega)\cdot p_\phi(\Omega)\right)d\Omega} \tag{3}$$

where:

i, j are two separate ports under investigation;

$$G_\theta(\Omega) = E_\theta(\Omega)\cdot E^*_\theta(\Omega) \tag{4}$$

and

$$G_\phi(\Omega) = E_\phi(\Omega)\cdot E^*_\phi(\Omega) \tag{5}$$

$E_{\theta i}(\Omega)$ and $E_{\phi i}(\Omega)$ are θ component and ϕ component of the electric field of Ant. i excited while other antennas are terminated with matched loads. $p_\theta(\Omega)$ and $p_\phi(\Omega)$ are the angular distribution of respective components, representing the propagation characteristics of the channel in where the antennas and array operate. Although the 3D uniform angular distribution assumption is always used in the literature, it would be important to investigate the ECC with certain angular distributions, especially for base station applications [41], [42]. XPD is the cross-polarization discrimination of the propagation channel and it is assumed as 1 in this design. Angle spread is an influencing factor in the value of ECC. The smaller the angle spread, the larger the value of ECC.

To comply with practical engineering habits, the coordinate system of the decoupled array is redefined as shown in Fig. 26 (a). Based on the coverage area of the three-sector base station antenna, the azimuth angle spread of the base station is less than 120 degrees. Therefore, we consider the azimuthal angle spread of the real environment and calculate the ECC for different azimuth spreads. Fig. 26 (b)–(e) show the ECC between port 3 and port 5 and between port 4 and port 6 with various angular spreads. Fig. 26 (b) and (c) show the variation of ECC between port 3 and port 5 when φ is in a fixed range and θ is varied. It can be seen that the change in θ has a small effect on the ECC. Fig. 26 (d) and (e) demonstrate the variation of port-to-port ECC as φ varies with θ in a fixed range. The ECC increases significantly as the range of φ decreases, but the ECC between port 1 and port 3 and ECC between port 4 and port 6 are less than 0.2 for φ in the range of $-60°$ to $60°$. It can be observed that the ECC of the decoupled MIMO antenna array is at a low level, which proves that the proposed decoupling method not only increases port isolation but also maintains a low correlation in space and eventually improves the system performance.

Table 3 shows the comparison between the proposed decoupling method and other related decoupling techniques.

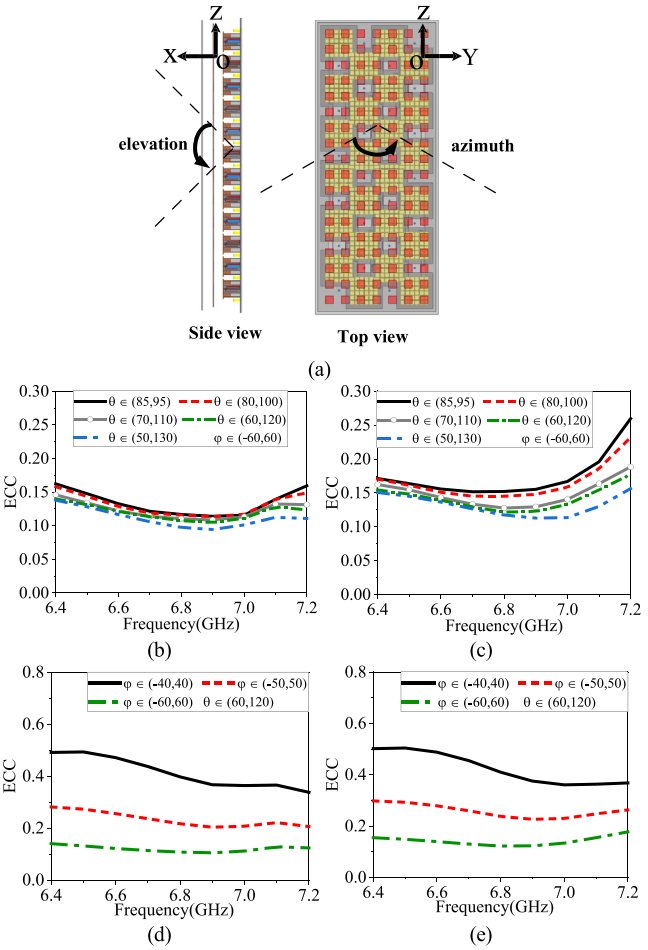

FIGURE 26. (a) 6 × 4 decoupled array coordinate system for ECC calculation. ECCs of different elevation angular spreads (θ) when φ is fixed between (b) ports 3 and 5, (c) ports 4 and 6. ECCs of different azimuth angular spreads (φ) when θ is fixed between (d) ports 3 and 5, (e) ports 4 and 6.

There are more studies on the technique of array decoupling with uniform arrangements, such as [4], [5], [32], [34] and [38]. Reference [38] used polarization selective partial reflection decoupling layers targeted to solve the E-plane and H-plane couplings of a one-dimensional line array, but the method is difficult to extend to the two-dimensional plane. References [29], [35] and [36] proposed decoupling methods on staggered arrays, with larger spacings and the application for more compact arrays is still to be investigated. Compared with other technologies, the systematic decoupling method proposed in this paper is suitable for the staggered array with power combiners, which has a much smaller interelement spacing.

IV. CONCLUSION

In this paper, a systematic array decoupling method using combinations of PRDLs and DDPs is proposed, which has been successfully applied to the compact U6G massive MIMO antenna array. Two layers of PRDLs and two types of DDPs are gradually introduced in the original array to control the magnitude and phase of major couplings with and without

TABLE 3. Comparison of the proposed decoupling structures and other decoupling techniques.

Ref.	Decoupling method	Array configuration	Bandwidth (GHz)	Antenna polarization	Spacing (center-to-center)	Array Configuration	Isolation (dB)	Power combiners
[5]	Split-ring resonator	1 × 4	3.4-3.8 (11%) ($\|S_{11}\|$<-15)	Dual	0.5 λ_0	Uniform	>25	w/o
[6]	Wave-trap structure	4 × 2	4.65-5.3 (13%) ($\|S_{11}\|$<-10)	Single	0.5 λ_0	Uniform	>23.5	w/o
[29]	ADS + staple-shaped phase compensation probe	4 × 4	3.3-3.8 (14%) ($\|S_{11}\|$<-15)	Dual	0.5 λ_0	Staggered	>25	w/o
[32]	Dielectric superstrate	2 × 2	3.3-3.8 (14%) $\|S_{11}\|$ (<-15)	Dual	0.53 λ_0	Uniform	>25	w/o
[34]	decoupling structure with polarization rotation	1 × 2	3.3-3.8 (14%) ($\|S_{11}\|$<-15)	Single	0.5 λ_0	Uniform	>27	w/o
[35]	Dual-Layer superstrate structure	3 × 3	3.4-4.2 (21%) ($\|S_{11}\|$<-12)	Dual	0.5 λ_0	Staggered	>23	w/o
[36]	Single Layer PRDL	4 × 4	1.7-2.3 (30%) ($\|S_{11}\|$<-15)	Dual	0.53 λ_0	Staggered	>25	w.
[38]	Polarization Sensitive PRDL	1 × 2	1.71-2.17(23.7%) ($\|S_{11}\|$<-12)	Dual	0.58 λ_0	Uniform	>21	w/o
Pro.	PRDLs + DDPs	6 × 4	6.4-7.2 (12%) ($\|S_{11}\|$<-12)	Dual	0.36 λ_0	Staggered	>21	w.

Note: λ_0 represents the free-space wavelengths of the center frequency.

power combiners. Through the cooperation of PRDLs and DDPs, the most eminent mutual couplings between adjacent columns are suppressed, and the port isolation is improved by 6-15 dB. Meanwhile, further investigation into the radiation performance of the array also shows great improvement.

The use of d-PRDLs in the design greatly speeds up the design process, meanwhile, shedding light on the basic working mechanism of the PRDL. It is promising to be applied in large-scale antenna arrays with restricted element spacing and hybrid MIMO beamforming architecture in future U6G or even millimeter wave communications.

ACKNOWLEDGMENT

The authors would like to thank Lu Zhang and Zexing Fan at Xi'an Lambda Communication Company Ltd. for assisting in prototype preparation and performance measurement. Meanwhile, Luyu Zhao and Huiqing Zhai want to express gratitude to the extraordinary engineers and administrative staff at Huawei Technologies Company Ltd., without whom this whole challenging project would be impossible to accomplish.

REFERENCES

[1] "3GPP commences 6GHz IMT-licensed spectrum standardizations." Accessed: Dec. 2022. [Online]. Available: https://telecomreviewafrica.com/index.php/en/articles/reports-and-covercov/2615–3gpp-commences-6-ghz-imt-licensed-spectrum-standardizatios

[2] "Final acts WRC-19." Accessed: Nov. 2019. [Online]. Available: https://www.itu.int/pub/R-ACT-WRC.14–2019/en

[3] E. G. Larsson, O. Edfors, F. Tufvesson, and T. L. Marzetta, "Massive MIMO for next generation wireless systems," *IEEE Commun. Mag.*, vol. 52, no. 2, pp. 186–195, Feb. 2014.

[4] M. A. Jensen and J. W. Wallace, "A review of antennas and propagation for MIMO wireless communications," *IEEE Trans. Antennas Propag.*, vol. 52, no. 11, pp. 2810–2824, Nov. 2004.

[5] M. Li, X. Chen, A. Zhang, W. Fan, and A. A. Kishk, "Split-ring resonator-loaded baffles for decoupling of dual-polarized base station array," *IEEE Antennas Wireless Propag. Lett.*, vol. 19, no. 10, pp. 1828–1832, Oct. 2020.

[6] Y. Zhang, S. Zhang, J. Li, and G. F. Pedersen, "A wavetrap-based decoupling technique for 45° polarized MIMO antenna arrays," *IEEE Trans. Antennas Propag.*, vol. 68, no. 3, pp. 2148–2157, Mar. 2020.

[7] L. Zhao, Y. He, G. Zhao, X. Chen, G.-L. Huang, and W. Lin, "Scanning angle extension of a millimeter-wave antenna array using electromagnetic band gap ground," *IEEE Trans. Antennas Propag.*, vol. 70, no. 8, pp. 7264–7269, Aug. 2022.

[8] E. Rajo-Iglesias, Ó. Quevedo-Teruel, and L. Inclan-Sanchez, "Mutual coupling reduction in patch antenna arrays by using a planar EBG structure and a multilayer dielectric substrate," *IEEE Trans. Antennas Propag.*, vol. 56, no. 6, pp. 1648–1655, Jun. 2008.

[9] H. S. Farahani, M. Veysi, M. Kamyab, and A. Tadjalli, "Mutual coupling reduction in patch antenna arrays using a UC-EBG superstrate," *IEEE Antennas Wireless Propag. Lett.*, vol. 9, pp. 57–59, 2010.

[10] D. Gao, Z.-X. Cao, S.-D. Fu, X. Quan, and P. Chen, "A novel slot-array defected ground structure for decoupling microstrip antenna array," *IEEE Trans. Antennas Propag.*, vol. 68, no. 10, pp. 7027–7038, Oct. 2020.

[11] Z. Niu, H. Zhang, Q. Chen, and T. Zhong, "Isolation enhancement for 1×3 closely spaced e-plane patch antenna array using defect ground structure and metal-vias," *IEEE Access*, vol. 7, pp. 119375–119383, 2019.

[12] B. Qian, X. Huang, X. Chen, M. Abdullah, L. Zhao, and A. A. Kishk, "Surrogate-assisted defected ground structure design for reducing mutual coupling in 2 × 2 microstrip antenna array," *IEEE Antennas Wireless Propag. Lett.*, vol. 21, no. 2, pp. 351–355, Feb. 2022.

[13] Y. Zhu, Y. Chen, and S. Yang, "Decoupling and low-profile design of dual-band dual-polarized base station antennas using frequency-selective surface," *IEEE Trans. Antennas Propag.*, vol. 67, no. 8, pp. 5272–5281, Aug. 2019.

[14] Y. He, Z. Pan, X. Cheng, Y. He, J. Qiao, and M. M. Tentzeris, "A novel dual-band, dual-polarized, miniaturized and low-profile base station antenna," *IEEE Trans. Antennas Propag.*, vol. 63, no. 12, pp. 5399–5408, Dec. 2015.

[15] Y. M. Pan, Y. Hu, and S. Y. Zheng, "Design of low mutual coupling dielectric resonator antennas without using extra decoupling element," *IEEE Trans. Antennas Propag.*, vol. 69, no. 11, pp. 7377–7385, Nov. 2021.

[16] J. Zhu and G. V. Eleftheriades, "A simple approach for reducing mutual coupling in two closely spaced metamaterial-inspired monopole antennas," *IEEE Antennas Wireless Propag. Lett.*, vol. 9, pp. 379–382, 2010.

[17] L. Chang, Y. Yu, K. Wei, and H. Wang, "Orthogonally-polarized dual antenna pair with high isolation and balanced high performance for 5G MIMO smartphone," *IEEE Trans. Antennas Propag.*, vol. 68, no. 5, pp. 3487–3495, May 2020.

[18] Y. Wang and Z. Du, "A wideband printed dual-antenna with three neutralization lines for mobile terminals," *IEEE Trans. Antennas Propag.*, vol. 62, no. 3, pp. 1495–1500, Mar. 2014.

[19] S. Su, C. Lee, and F.-S. Chang, "Printed MIMO-antenna system using neutralization-line technique for wireless USB-dongle applications," *IEEE Trans. Antennas Propag.*, vol. 60, no. 2, pp. 456–463, Feb. 2012.

[20] Y. He, S. Lv, L. Zhao, G.-L. Huang, X. Chen, and W. Lin, "A compact dual-band and dual-polarized millimeter-wave beam scanning antenna array for 5G mobile terminals," *IEEE Access*, vol. 9, pp. 109042–109052, 2021.
[21] B. K. Lau and J. B. Andersen, "Simple and efficient decoupling of compact arrays with parasitic scatterers," *IEEE Trans. Antennas Propag.*, vol. 60, no. 2, pp. 464–472, Feb. 2012.
[22] S. Zhang, X. Chen, and G. F. Pedersen, "Mutual coupling suppression with decoupling ground for massive MIMO antenna arrays," *IEEE Trans. Veh. Technol.*, vol. 68, no. 8, pp. 7273–7282, Aug. 2019.
[23] L. Zhao and K. Wu, "A dual-band coupled resonator decoupling network for two coupled antennas," *IEEE Trans. Antennas Propag.*, vol. 63, no. 7, pp. 2843–2850, Jul. 2015.
[24] K. Lin, C. Wu, C. Lai, and T. Ma, "Novel dual-band decoupling network for two-element closely spaced array using synthesized microstrip lines," *IEEE Trans. Antennas Propag.*, vol. 60, no. 11, pp. 5118–5128, Nov. 2012.
[25] C.-D. Xue, X. Y. Zhang, Y. F. Cao, Z. Hou, and C. F. Ding, "MIMO antenna using hybrid electric and magnetic coupling for isolation enhancement," *IEEE Trans. Antennas Propag.*, vol. 65, no. 10, pp. 5162–5170, Oct. 2017.
[26] L. Sun, Y. Li, and Z. Zhang, "Decoupling between extremely closely spaced patch antennas by mode cancellation method," *IEEE Trans. Antennas Propag.*, vol. 69, no. 6, pp. 3074–3083, Jun. 2021.
[27] T. Pei, L. Zhu, J. Wang, and W. Wu, "A Low-Profile decoupling structure for mutual coupling suppression in MIMO patch antenna," *IEEE Trans. Antennas Propag.*, vol. 69, no. 10, pp. 6145–6153, Oct. 2021.
[28] W. Yang, L. Chen, S. Pan, W. Che, and Q. Xue, "Novel decoupling method based on coupling energy cancellation and its application in 5G dual-polarized high-isolation antenna array," *IEEE Trans. Antennas Propag.*, vol. 70, no. 4, pp. 2686–2697, Apr. 2022.
[29] C. Wei, Z. Zhang, and K. Wu, "Phase compensation for decoupling of large-scale staggered dual-polarized dipole array antennas," *IEEE Trans. Antennas Propag.*, vol. 68, no. 4, pp. 2822–2831, Apr. 2020.
[30] F. Liu, J. Guo, L. Zhao, G.-L. Huang, Y. Li, and Y. Yin, "Ceramic superstrate-based decoupling method for two closely packed antennas with cross-polarization suppression," *IEEE Trans. Antennas Propag.*, vol. 69, no. 3, pp. 1751–1756, Mar. 2021.
[31] Y. Liu and L. Zhao, "Artificial and Natural dielectric layers for mutual coupling reduction of massive MIMO antennas," in *Proc. IEEE Int. Symp. Antennas Propag. North Amer. Radio Sci. Meeting*, 2020, pp. 1913–1914.
[32] Y. Da, Z. Zhang, X. Chen, and A. A. Kishk, "Mutual coupling reduction with dielectric superstrate for base station arrays," *IEEE Antennas Wireless Propag. Lett.*, vol. 20, no. 5, pp. 843–847, May 2021.
[33] M. Li and S. Cheung, "Isolation enhancement for MIMO dielectric resonator antennas using dielectric superstrate," *IEEE Trans. Antennas Propag.*, vol. 69, no. 7, pp. 4154–4159, Jul. 2021.
[34] B. Liu, X. Chen, J. Tang, A. Zhang, and A. A. Kishk, "Co- and cross-polarization decoupling structure with polarization rotation property between linearly polarized dipole antennas with application to decoupling of circularly polarized antennas," *IEEE Trans. Antennas Propag.*, vol. 70, no. 1, pp. 702–707, Jan. 2022.
[35] Y. Li and Q.-X. Chu, "Dual-layer superstrate structure for decoupling of dual-polarized antenna arrays," *IEEE Antennas Wireless Propag. Lett.*, vol. 21, no. 3, pp. 521–525, Mar. 2022.
[36] J. Guo, F. Liu, L. Zhao, G.-L. Huang, W. Lin, and Y. Yin, "Partial reflective decoupling superstrate for dual-polarized antennas application considering power combining effects," *IEEE Trans. Antennas Propag.*, vol. 70, no. 10, pp. 9855–9860, Oct. 2022.
[37] T. Liu and L. Zhao, "A compact large-scale antenna with high isolation for base station applications," in *Proc. IEEE Int. Symp. Antennas Propag. USNC-URSI Radio Sci. Meeting (APS/URSI)*, 2021, pp. 935–936.
[38] G. Zhao, T. Liu, J. Jiang, L. Zhao, G.-L. Huang, and W. Lin, "Polarization selective partial reflective decoupling layers for mutual coupling reduction of two-closely spaced dual-polarized antennas," *IEEE Trans. Antennas Propag.*, vol. 70, no. 11, pp. 11205–11210, Nov. 2022.
[39] H. Yang et al., "Aperture reduction using downward and upward bending arms for dual-polarized quadruple-folded-dipole antennas," *IEEE Antennas Wireless Propag. Lett.*, vol. 22, no. 3, pp. 645–649, Mar. 2023.
[40] Z. Li, K. Aydin, and E. Ozbay, "Determination of the effective constitutive parameters of bianisotropic metamaterials from reflection and transmission coefficients," *Phys. Rev. E, Stat. Phys. Plasmas Fluids Relat. Interdiscip. Top.*, vol. 79, Feb. 2009, Art. no. 26610.
[41] Y. Wang et al., "Improvement of diversity and capacity of MIMO system using scatterer array," *IEEE Trans. Antennas Propag.*, vol. 70, no. 1, pp. 789–794, Jan. 2022.
[42] M. Li, X. Chen, A. Zhang, A. A. Kishk, and W. Fan, "Reducing correlation in compact arrays by adjusting near-field phase distribution for MIMO applications," *IEEE Trans. Veh. Technol.*, vol. 70, no. 8, pp. 7885–7896, Aug. 2021.

TING LIU was born in Shaanxi, China, in 1998. She received the B.S. degree from Xidian University, Xi'an, in 2020, where she is currently pursuing the M.S. degree in electromagnetic fields and microwave technology. Her research interests include the decoupling of antenna arrays and the miniaturization of antenna elements.

JIAYUE JIANG received the B.S. degree from Xidian University, Xi'an, China, in 2020, where he is currently pursuing the Ph.D. degree in electromagnetic field and microwave technology. His research interests include antenna decoupling, the design of compact base station antenna arrays, and improvement of antenna array performance.

LUYU ZHAO (Senior Member, IEEE) was born in Xi'an, China, in 1984. He received the B.Eng. degree from Xidian University, Xi'an, in 2007, and the Ph.D. degree from The Chinese University of Hong Kong, Shatin, Hong Kong, in 2014.

He has been an Associate Professor with the National Key Laboratory of Antennas and Microwave Technology, Xidian University since 2016. From 2007 to 2009, he was a Research Assistant with the Key Laboratory of Antennas and Microwave Technology, Xidian University, where he was involved with software and hardware implementation of RF identification technologies. From 2014 to 2015, he was a Postdoctoral Fellow with The Chinese University of Hong Kong, Shatin. From October 2015 to October 2016, he was with Wyzdom Wireless Company Ltd., where he was a Co-Founder and a CTO. In 2019, he founded Xi'an Lambda Communication Company Ltd., and served as a CTO since then. He has authored or coauthored over 50 papers in referred journals and holds three U.S. nonprovisional patents as well as more than ten Chinese invention patents. He has coauthored three books and participated in one national standard. His current research interests include the design and application of multiple antenna systems for next-generation mobile communication systems, millimeter wave and terahertz antenna arrays and corresponding measurement techniques, metamaterial-based or inspired antenna arrays, intelligent surfaces, and innovative passive RF and microwave components and systems.

Prof. Zhao was the recipient of the Best Student Paper Award of the 2013 IEEE 14th HK AP/MTT Postgraduate Conference, the Honorable Mention Award of the 2017 Asia–Pacific Conference on Antenna and Propagation, the Best Paper Award of IEEE ICEICT 2019, and the Third Prize of Student Paper Competition in ACES-China 2021. He is currently serving as an Associate Editor for the IEEE ACCESS. He is also appointed as the corresponding expert of *Frontiers of Information Technology and Electronic Engineering*. He is a Senior Member of the China Institute of Communication.

GE ZHAO (Graduate Student Member, IEEE) received the B.S. degree in electronic information science and technology from Southwest Jiaotong University, Chengdu, China, in 2016, and the M.S. degree in electromagnetic field and microwave technology from Xidian University, Xi'an, China, in 2019, where she is currently pursuing the Ph.D. degree. Her main research interests include metamaterial antenna and antenna decoupling technology. She won the Cool Antenna Award in the 2020 ISAP Student Design Contest.

HUIQING ZHAI (Member, IEEE) was born in Jilin, China. He received the Ph.D. degree in electromagnetic fields and microwave technology from Xidian University, Xi'an, China, in 2004. From 2005 to 2008, he was a JSPS Research Fellow with Tohoku University, Sendai, Japan. From 2008 to 2010, he was a Research Fellow with the University of Texas at Arlington, Arlington, TX, USA. Since 2019, he has been the Head of the Electromagnetic Field and Microwave Engineering Department, Xidian University, where he is currently a Full Professor and a Ph.D. Supervisor. He has authorized or coauthored over 100 papers in referred journals, and over ten authorized invention patents. His current research interests include antennas for wireless communication, electromagnetic materials, electromagnetic detection, and electromagnetic invisibility cloaking.

YUAN-MING CAI (Member, IEEE) received the B.S. degree in electronic information engineering and the Ph.D. degree in electromagnetic wave and microwave technology from Xidian University, Xi'an, China, in 2011 and 2016, respectively.

He is currently an Associate Professor with the National Key Laboratory of Science and Technology on Antennas and Microwaves, Xidian University. His research interests include multiband and wideband antennas, antenna arrays, and reconfigurable antennas.

TEYAN CHEN received the B.Sc. degree from the University of Central Lancashire, Preston, U.K., in 2005, and the M.Sc. and Ph.D. degrees in electronic engineering from the University of York, York, U.K., in 2006 and 2011, respectively. In 2012, he joined Huawei Technologies Company Ltd., where he worked on various research projects for next-generation wireless communication systems. His research interests are within the areas of wireless communications and signal processing.

WENWEI (WILLIAM) XU (Senior Member, IEEE) is the Huawei's Director of the Board and the Chair of Huawei's Scientist Advisory Committee. He is responsible for Huawei's cooperation with universities and research institutions as well as for investment in advanced technologies. He also provides consultation and advises on technology and promotes the alignment and closer integration of industrial challenges and academic research. He joined Huawei's Research and Development Department in 1991. He has led the research and development of numerous key products, including Huawei's first generation of public program-controlled switches, the first global system for mobile communications, and the first data center core switch. He has previously served as the General Manager of Wireless R&D, the President of Research, the President of the European Area, the Chief Sales and Service Officer, the Founding President of HiSilicon, the Founding CEO of the Enterprise BG, and the Chairman of the Investment Review Board. He has extensive experience in research and development, market development, strategy development and execution, marketing, industry development, and technology portfolio planning. He has been instrumental in Huawei's growth from a startup in China to a major global company.